Fiber in-line Fabry–Pérot interferometer for simultaneous measurement of reflective index and temperature

Xiaoqi Ni (倪小琦), Ming Wang (王 鸣)*, and Dongmei Guo (郭冬梅)

Jiangsu Key Laboratory on Opto-Electronic Technology, School of Physical Science and Technology, Nanjing Normal University, Nanjing 210023, China

**Corresponding author: wangming@njnu.edu.cn*

Received December 11, 2015; accepted February 23, 2016; posted online April 6, 2016

A fiber in-line Fabry–Pérot interferometer is presented. The sensing head consists of a micro ellipsoidal air cavity and a small section of solid-core photonic crystal fiber. The reflective index (RI) and temperature can be interrogated simultaneously through a fast Fourier transform and by tracing the dip wavelength shift of the reflective spectrum. Experimental results show that the RI amplitude and wavelength sensitivities are 5.30/RIU and 8.46×10^{-1} nm/RIU in the range from 1.34 to 1.43, and the temperature amplitude and wavelength sensitivities are 6.8×10^{-4}/°C and 2.48×10^{-3} nm/°C in the range from 15°C to 75°C, respectively. Easy fabrication, a simple system, and simultaneous measurement make it appropriate for dual-parameter sensing application.

OCIS codes: 280.4788, 060.2370.

doi: 10.3788/COL201614.050601.

The measurement of reflective index (RI) has played an important role in physical, chemical, and biomedical areas. The optical fiber-based RI sensors have been intensively investigated and widely applied due to their unique advantages such as simplicity, immunity to electromagnetic interference, corrosion resistance, and remote sensing capability. Most of them are based on fiber gratings, Fabry–Pérot (FP) or Mach–Zehnder (MZ) interferometer, micro fiber, selectively infiltrated photonic crystal fiber (PCF) coupler, deposition of a thin film over the sensing element, and many other structures[1–11]. The FP interferometer (FPI)-based sensors have been much more extensively studied owing to their characteristics of simple configurations, compactness, stable performances, and endurance for high temperature and high pressure environments, etc. RI sensing cannot be carried out reliably without the simultaneous measurement of temperature. In recent years, optical fiber-based RI sensors with temperature compensation have been extensively investigated[5,7,8,12–14].

In this Letter, an FPI is presented. The sensing head of the interferometer consists of a closed air cavity and a section of PCF. The former responds to the envelope of the reflective spectrum, and the latter contributes to the high-frequency fringe spectrum. The spectral response of the interferometer with different lengths of PCF is analyzed. The frequency characteristics of reflective spectra when the interferometer is dipped into solutions with different RIs are studied. The influence of temperature on reflective spectra is also studied. Taking interaction into consideration, a matrix equation is used to demodulate RI and temperature simultaneously.

The FPI was made by splicing a standard single mode fiber (SMF) with a solid-core PCF whose cross section is shown in Fig. 1(a) (core diameter: 7.0 μm, cladding diameter: 125 μm). The splicing was performed on a fusion splicer (Fujikura 80S) and the discharge power and time were −40 dB and 1000 ms, respectively. The discharge position was on the SMF, about 100 μm from the end, in order not to destroy the end face of the PCF. Such fusion parameters ensure complete collapsing of the air holes in a limited region. After three discharge times, air holes in the cladding of the PCF collapsed and an elliptical air cavity was formed in the fiber. The collapsed region can be regarded as pure silica. Subsequently, the PCF was cut off with a small section remaining, as shown in Fig. 1(b). An optical sensing analyzer si720 provided by Micron Optics was used to act as both the light source and the spectral receiver. The scanning laser ranging from 1510 to 1590 nm was launched to the sensor from the SMF. The reflective spectra before cleaving (depicted with a black solid line), and when the remaining PCF are 1 and 9 mm after cleaving (dotted in blue and red, respectively), are shown in Fig. 2.

We found out that before cleaving the reflective spectrum is influenced only by the closed air cavity. Taking

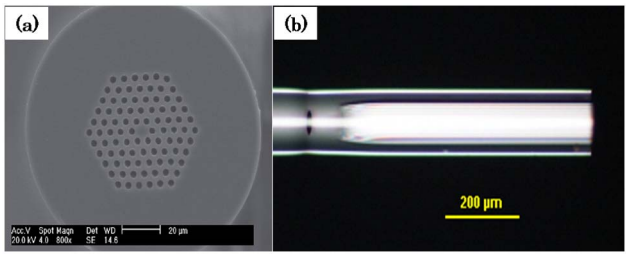

Fig. 1. Microscopic image of (a) cross-sectional image of PCF and (b) sensing head.

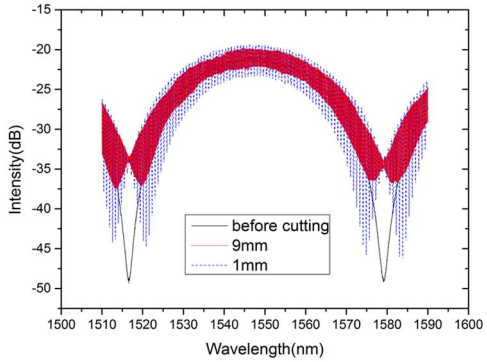

Fig. 2. Reflective spectra of sensors with different lengths of PCF.

both dips as λ_1 and λ_2, we calculated that the length of the air cavity is about 19.1 μm by using

$$L = \frac{\lambda_1 \lambda_2}{2n(\lambda_2 - \lambda_1)}, \tag{1}$$

which is almost the same as the measured value (18.85 μm). However, the other cavity was formed when a certain length of PCF remained after cleaving. The reflective spectra consist of an envelope and a high-frequency fringe spectrum whose frequency varies with the length of the remaining PCF. In order to find out where the fringe spectrum comes from, we analyzed the schematic diagram of the sensing head and the propagation of the light.

As shown in Fig. 3, after being reflected by the air cavity, the rest of the incident light is coupled to the PCF through the collapsed region. Lots of higher modes are excited at the beginning of the PCF, including the cladding modes. But the cladding modes vanish gradually through the propagation distance due to the power dissipation. As a result, the guided modes propagating in the PCF are the core modes, including the high-order modes. They are reflected by the PCF end face cleavage, and are coupled to the SMF again through the collapsed region. Taking the interference between the fundamental mode (LP_{01}) and the high-order mode (LP_{31})[15] into consideration, we calculated that the FP cavity should be 412 mm ($n = 3.51 \times 10^{-2}$[15]) when the interference spectrum is the same as the one dotted in red in Fig. 2. But it was not coincident with the experimental result (9 mm). So we inferred that the fringe spectrum was caused by the silica cavity (L_2), which was composed of the collapsed

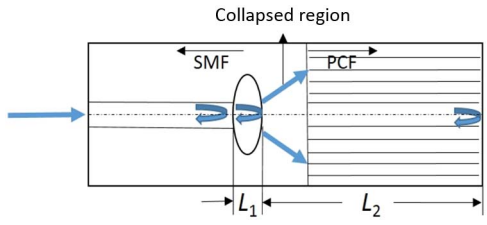

Fig. 3. Schematic diagram of the sensing head.

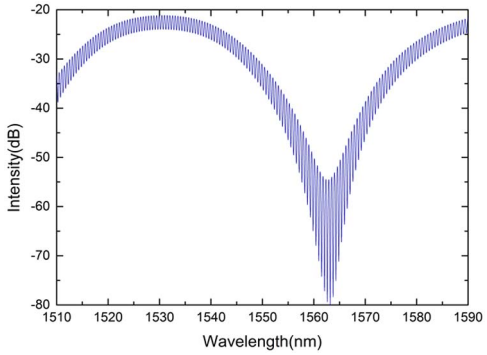

Fig. 4. Simulated reflective spectrum of the interferometer.

region and the PCF, as illustrated in Fig. 3. With $n = n_{\text{silica}} = 1.457$, we calculated that the cavity length should be 9.99 mm, which was well coincident with L_2 in the experiment (9.78 mm).

There are three reflection surfaces in the sensing head, as follows: SMF-air, air-silica, silica-surrounding with power reflection coefficients of R_1, R_2, and R_3, respectively. R_1 and R_2 are equal to $(n_0-1)^2/(n_0+1)^2 = 0.034$, $R_3 = (n_0 - n_{\text{Liq}})^2/(n_0 + n_{\text{Liq}})^2$, with n_0 being the RI of pure silica and n_{Liq} being the RI of the measured solution. The total reflected field from the sensor is given approximately by the sum of the first-order reflected fields from the three surfaces. The total contribution from the high-order reflections is less than 0.1% because of the low reflection coefficients and therefore can be neglected[6]. So the normalized reflection spectrum $R(\lambda)$ is obtained as follows[6,16]:

$$\begin{aligned} R(\lambda) = |E_r/E_i|^2 &= R_1 + (1-\alpha)^2(1-R_1)^2 R_2 \\ &+ (1-\alpha)^2(1-\gamma)^2(1-R_1)^2(1-R_2)^2 R_3 \\ &- 2\sqrt{R_1 R_2}(1-\alpha)(1-R_1)\cos(4\pi L_1/\lambda) \\ &- 2\sqrt{R_1 R_3}(1-\alpha)(1-\gamma)(1-R_1)(1-R_2) \\ &\times \cos[4\pi(L_1 + n_0 L_2)/\lambda)] \\ &+ 2\sqrt{R_2 R_3}(1-\alpha)^2(1-\gamma)(1-R_1)^2(1-R_2) \\ &\times \cos(4\pi n_0 L_2/\lambda), \end{aligned} \tag{2}$$

where E_i is the incident wave field, E_r is the reflected wave field, α and γ are the diffraction loss factors of air cavity and silica cavity, respectively. A phase shift of π takes place at the reflection surface of air and fiber because light is reflected from an optically dense medium to a thinner medium. As a result, if the refractive index of the solution to be measured (n_{Liq}) is bigger than n_0, there is also a π phase shift at the reflection surface of the PCF. From Eq. (2), we find out that the reflection coefficient R_3, which depends on n_{Liq}, only affects the amplitude of $R(\lambda)$. So when the sensor is dipped into different solutions, the fringe contrast of the reflective spectrum will change, whereas the phase will remain unchanged.

The reflective interference spectrum is simulated with the parameters $L_1 = 18.75$ μm, $L_2 = 1531$ μm, $n_0 = 1.457$,

$R_1 = R_2 = 0.034$, and $R_3 = 0.002$ with $n_{\mathrm{Liq}} = 1.33$, $\alpha = 0.2$, $\gamma = 0.32$. The simulated result in wavelength range from 1510 to 1590 nm is depicted in Fig. 4, from which we can see that the reflective spectrum mainly consists of a low-frequency envelope and a high-frequency waveform. To analyze the characteristics of the interference pattern, the wavelength spectrum was Fourier transformed to a spatial frequency. The reflective spectra with n_{Liq} in the range from 1.33 to 1.45 were analyzed after a fast Fourier transform (FFT).

Taking the parameter "Amplitude" as the Y axis, the FFT results in the spatial frequency domain are shown in Fig. 5. Amplitude is defined as $\sqrt{\mathrm{Re}^2 + \mathrm{Im}^2}/n$, where Re and Im are the real and imaginary part of the FFT data, and n is the number of sample points, respectively.

From Fig. 5, we can see that the first several peaks in the spatial frequency domain, which correspond to interferences in the air cavity, do not change with n_{Liq}. But the peak near the frequency of about 1.8 nm^{-1}, which corresponds to interferences in the cavity of silica, decreases when n_{Liq} increases. The relationship between the amplitude peak (P) near the frequency of about 1.8 nm^{-1} and the RI of the solution is depicted in Fig. 6, from which we can see that the simulated P has a linear relationship with the RI.

Given that the RI of a material itself exhibits a dependence on temperature, RI sensing cannot be carried out reliably without the simultaneous measurement of temperature. When temperature changes, the dip wavelength (λ_{dip}) of the reflective optical spectrum will shift and the amplitude peaks of the frequency spectrum will also change. If both parameters are perturbed simultaneously by the RI and temperature, the variation of the dip wavelength $\Delta\lambda_{\mathrm{dip}}$ caused by the temperature and RI can be expressed as[12]

$$\Delta\lambda_{\mathrm{dip}} = K_{\lambda,T}\,\Delta T + K_{\lambda,\mathrm{RI}}\Delta\mathrm{RI}, \tag{3}$$

where $K_{\lambda,T}$ is the sensitivity coefficient of the temperature and the unit is nm/°C, and $K_{\lambda,\mathrm{RI}}$ is the sensitivity coefficient of RI and the unit is nm/RIU. The variation of the

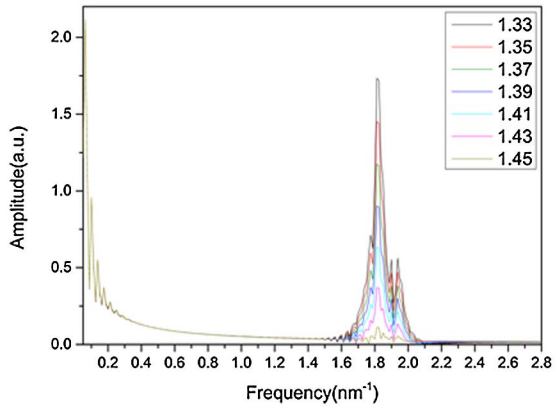

Fig. 5. Simulated FFT results of spectral responses with different n_{Liq}.

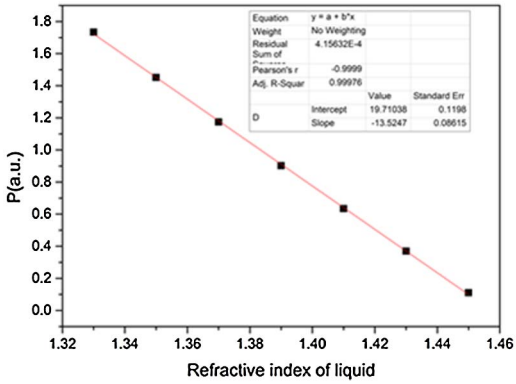

Fig. 6. Simulated relationship between the P and RI of the solution.

amplitude peak (ΔP) of the FFT results caused by the variation in temperature and RI can be expressed as

$$\Delta P = K_{P,T}\Delta T + K_{P,\mathrm{RI}}\Delta\mathrm{RI}, \tag{4}$$

where $K_{P,T}$ is the sensitivity coefficient of the temperature with units of /°C, and $K_{P,\mathrm{RI}}$ is the sensitivity coefficient of RI with units of /RIU. The equation of the sensitivity matrix can be written as[12,13]

$$\begin{bmatrix} \Delta\lambda_{\mathrm{dip}} \\ \Delta P \end{bmatrix} = \begin{bmatrix} K_{\lambda,T} & K_{\lambda,\mathrm{RI}} \\ K_{P,T} & K_{P,\mathrm{RI}} \end{bmatrix} \begin{bmatrix} \Delta T \\ \Delta\mathrm{RI} \end{bmatrix}. \tag{5}$$

The equation of the sensitivity matrix can be transposed as

$$\begin{bmatrix} \Delta T \\ \Delta\mathrm{RI} \end{bmatrix} = \frac{1}{D} \begin{bmatrix} K_{P,\mathrm{RI}} & -K_{\lambda,\mathrm{RI}} \\ -K_{P,T} & K_{\lambda,T} \end{bmatrix} \begin{bmatrix} \Delta\lambda_{\mathrm{dip}} \\ \Delta P \end{bmatrix}, \tag{6}$$

where $D = K_{\lambda,T}K_{P,\mathrm{RI}} - K_{P,T}K_{\lambda,\mathrm{RI}}$, and $K_{\lambda,T}$, $K_{\lambda,\mathrm{RI}}$, $K_{P,T}$, and $K_{P,\mathrm{RI}}$ are regarded as constant values and can be determined by measuring the temperature and wavelength response separately for $\Delta\lambda_{\mathrm{dip}}$ and ΔP. The temperature and RI variations can thus be evaluated by Eq. (6).

Several all-fiber optical FPIs with different lengths of air cavity and PCF were fabricated. Two reflective spectra in the air at 10°C are shown in Fig. 7, with parameters as follows: for sensor1, $L_1 = 15.6$ μm, $L_2 = 925$ μm; for sensor2, $L_1 = 6.2$ μm, $L_2 = 1400$ μm. The solid line represents the reflective spectrum of sensor1 and the dotted line represents sensor2. To calibrate the sensor, we immersed sensor1 into the prepared sugar solution with different RI, and we found that the fringe contrast of the reflective spectrum decreases with RI. The FFT results of the reflective spectra with different RIs are shown in Fig. 8.

Subsequently, the sensor was placed in an oven and the temperature was twice increased from 15°C to 75°C and then decreased to 15°C.

Assuming ΔP_{RI} is the difference between the measured P in the air and in different solutions, ΔRI is the difference

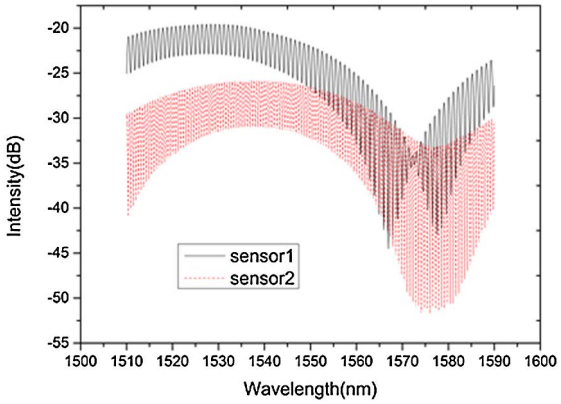

Fig. 7. Reflective spectra of two sensors with different L_1 and L_2.

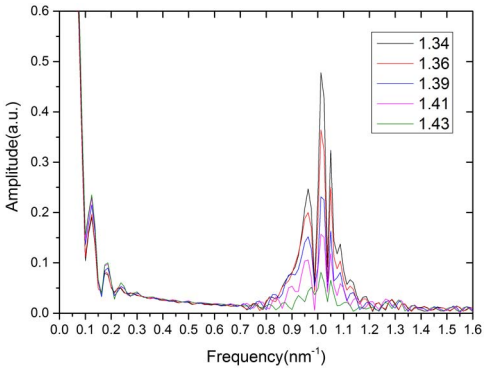

Fig. 8. FFT results of spectral responses with different solution RIs.

between the RI of the solution and the air, the experimental ΔP_{RI} were dotted in Fig. 9. Assuming ΔP_T is the difference of the measured P at different temperatures and at 10°C, the experimental ΔP_T values were marked with square points in Fig. 9. After linear fitting, we found out that the parameter ΔP increases almost linearly with ΔRI, with the sensitivity of 5.30/RIU, and ΔP also increases linearly with ΔT, with the sensitivity of 6.80×10^{-4}/°C. Consequently, the parameters $K_{P,T}$

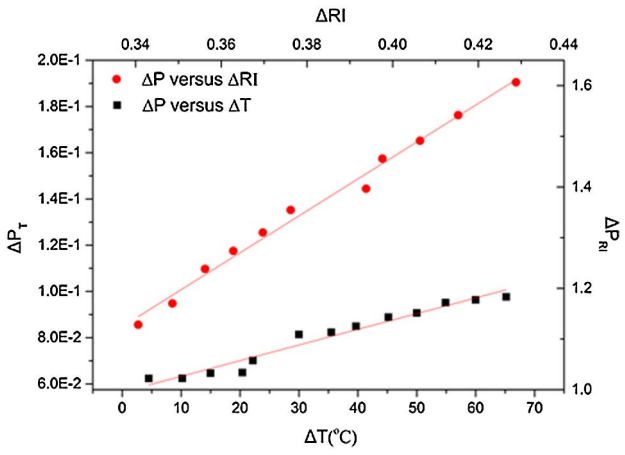

Fig. 9. Comparison of ΔP caused by ΔRI and ΔT.

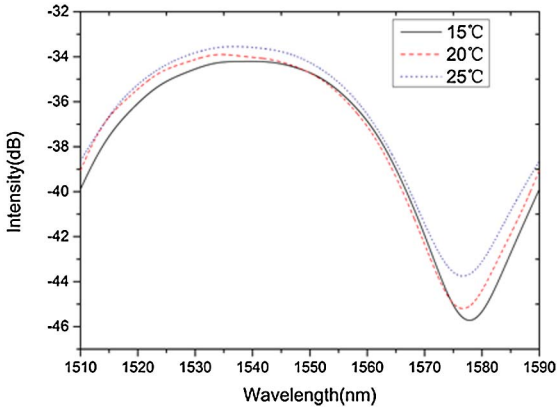

Fig. 10. Reflective spectra at different temperatures.

and $K_{P,\mathrm{RI}}$ in Eq. (5) are 6.80×10^{-4}/°C and 5.30/RIU, respectively. In this Letter, the solution samples were characterized through an Abbe refractometer.

The relationship between $\Delta\lambda_{\mathrm{dip}}$ and ΔRI, together with the relationship between $\Delta\lambda_{\mathrm{dip}}$ and ΔT were explored in this Letter. The reflective spectra of the sensor after a low-pass filter with a cutoff frequency of 0.15 Hz at temperatures of 15°C, 20°C, and 25°C were shown in Fig. 10. The dip wavelength shifts to short wavelength with the increase of temperature. Assuming $\Delta\lambda_{\mathrm{RI}}$ is the wavelength shift caused by ΔRI, the experimental $\Delta\lambda_{\mathrm{RI}}$ were dotted in Fig. 11. Assuming $\Delta\lambda_T$ is the wavelength shift caused by ΔT, the experimental $\Delta\lambda_T$ were marked with square points in Fig. 11. After linear fitting, we found out that the parameter $\Delta\lambda_{\mathrm{dip}}$ increases almost linearly with ΔRI, with a sensitivity of 8.46×10^{-1} nm/RIU and $\Delta\lambda_{\mathrm{dip}}$ also increases linearly with ΔT with a sensitivity of 2.48×10^{-3} nm/°C. Consequently, the parameters $K_{\lambda,T}$ and $K_{\lambda,\mathrm{RI}}$ in Eq. (5) are 2.48×10^{-3} nm/°C and 8.46×10^{-1} nm/RIU, respectively, and Eq. (5) can be written as follows:

$$\begin{bmatrix} \Delta\lambda_{\mathrm{dip}} \\ \Delta P \end{bmatrix} = \begin{bmatrix} 2.48 \times 10^{-3} & 8.46 \times 10^{-1} \\ 6.80 \times 10^{-4} & 5.30 \end{bmatrix} \begin{bmatrix} \Delta T \\ \Delta\mathrm{RI} \end{bmatrix}. \quad (7)$$

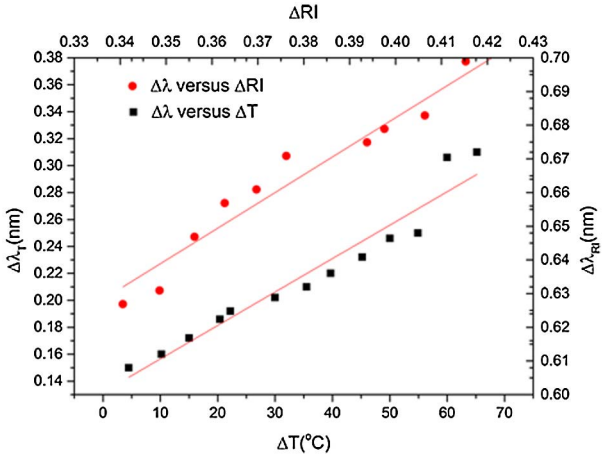

Fig. 11. Comparison of $\Delta\lambda_{\mathrm{dip}}$ caused by ΔRI and ΔT.

Equation (6) can be written as

$$\begin{bmatrix} \Delta T \\ \Delta \mathrm{RI} \end{bmatrix} = \begin{bmatrix} 4.05 \times 10^{2} & -6.55 \times 10^{-4} \\ -5.25 \times 10^{-3} & 2.00 \times 10^{-6} \end{bmatrix} \begin{bmatrix} \Delta\lambda_{\mathrm{dip}} \\ \Delta P \end{bmatrix}. \quad (8)$$

Equation (8) can be applied to simultaneously determine the surrounding RI and temperature, as long as the wavelength shift $\Delta\lambda_{\mathrm{dip}}$ and ΔP are measured.

In conclusion, a simple optical sensor is proposed and demonstrated that can be used to simultaneously measure RI and temperature. The sensing head is made by splicing a small section of PCF with SMF, with an ellipsoid air cavity reserved. The interference model is analyzed theoretically and verified experimentally. ΔP from the FFT analysis and $\Delta\lambda_{\mathrm{dip}}$ of the envelope after the FFT low-pass filter can be measured. An amplitude sensitivity of 5.30/RIU after the FFT and a wavelength sensitivity of 8.46×10^{-1} nm/RIU are experimentally achieved over the RI range from 1.34 to 1.43. For temperature measurements, an amplitude sensitivity of 6.80×10^{-4}/°C and a wavelength sensitivity of 2.48×10^{-3} nm/°C are achieved. Easy fabrication, low cost, good temperature compensation, and dual-parameter measurement make it appropriate for practical applications.

This work was supported by the National Natural Science Foundation of China (Nos. 61178044 and 51405240), the Natural Science Foundation of Jiangsu Province of China (No. BK20140925), the Major Project of the Nature Science Research for Colleges and Universities in Jiangsu Province (No. 15KJA140002), the Program of Natural Science Research of the Jiangsu Higher Education Institutions of China (No. 14KJB510015), and the University Postgraduate Research and Innovation Project of Jiangsu Province (No. 1812000002A422).

References

1. W. Daisy, B. Xiaoyi, and C. Liang, Photon. Res. **2**, 1 (2014).
2. X. Jiang, D. Chen, J. Shao, G. Feng, and J. Yang, Chin. Opt. Lett. **12**, S10609 (2014).
3. R. Jha, J. Villatoro, and G. Badenes, Appl. Phys. Lett. **93**, 191106 (2008).
4. L. Li, D. Zhang, X. Wen, and S. Peng, Chin. Opt. Lett. **13**, 100601 (2015).
5. T. Wang and M. Wang, IEEE Photon. Technol. Lett. **19**, 24 (2012).
6. M. Jiang, Q.-S. Li, J.-N. Wang, Z. Jin, Q. Sui, Y. Ma, Y. Ma, J. Shi, F. Zhang, L. Jia, W.-G. Yao, and W.-F. Dong, Opt. Express **3**, 21 (2013).
7. P. Wang, L. Bo, C. Guan, Y. Semenova, Q. Wu, G. Brambilla, and G. Farrell, Opt. Lett. **19**, 38 (2013).
8. H. Liang, W. Zhang, W. Zhang, H. Wang, P. Geng, S. Zhang, S. Gao, C. Yang, and J. Li, Opt. Lett. **20**, 38 (2013).
9. S. Gao, W. Zhang, Z.-Y. Bai, H. Zhang, W. Lin, L. Wang, and J. Li, J. Lightwave Technol. **9**, 32 (2014).
10. T. Han, Y.-G. Liu, Z. Wang, Z. Wu, S. Wang, and S. Li, Opt. Express **12**, 20 (2013).
11. C. R. Liao, D. N. Wang, and Y. Wang, Opt. Lett. **5**, 38 (2013).
12. H. Liu, H. Liang, M. Sun, K. Ni, and Y. Jin, IEEE Sens. J. **3**, 14 (2014).
13. X. Xue, W. Zhang, H. Zhang, S. Gao, P. Geng, Z. Bai, and J. Li, Meas. Sci. Technol. **24**, 065103 (2013).
14. R. Wang and X. Qiao, Appl. Opt. **32**, 53 (2014).
15. J. Zheng, P. Yan, Y. Yu, Z. Ou, J. Wang, X. Chen, and C. Du, Opt. Commun. **297**, 7 (2013).
16. Y. J. Rao, M. Deng, D.-W. Duan, and T. Zhu, Sens. Actuators A. **148**, 33 (2008).